Complex particle acceleration processes in the hotspots of 3C 105 and 3C 445*

M. Orienti[1,2]†, M.A. Prieto[3], G. Brunetti[2], K.-H. Mack[2], F. Massaro[4], D.E. Harris[4]

[1] *Dipartimento di Astronomia, Università di Bologna, via Ranzani 1, I-40127, Bologna, Italy*
[2] *Istituto di Radioastronomia - INAF, Via P. Gobetti 101, I-40129 Bologna, Italy*
[3] *Instituto de Astrofísica de Canarias, c/ Vía Láctea s/n, E-38205 La Laguna (Tenerife), Spain*
[4] *Smithsonian Astrophysical Observatory, 60 Garden Street, Cambridge, MA 02138, USA*

ABSTRACT

We investigate the nature of the broad-band emission associated with the low-power radio hotspots 3C 105 South and 3C 445 South. Both hotspot regions are resolved in multiple radio/optical components. High-sensitivity radio VLA, NIR/optical VLT and HST, and X-ray *Chandra* data have been used to construct the multi-band spectra of individual hotspot components. The radio-to-optical spectra of both hotspot regions are well fitted by a synchrotron model with steep spectral indices ~ 0.8 and break frequencies between $10^{12} - 10^{14}$ Hz. 3C 105 South is resolved in two optical components: a primary one, aligned with the jet direction and possibly marking the first jet impact with the surrounding medium, and a secondary, further out from the jet and extended in a direction perpendicular to it. This secondary region is interpreted as a splatter-spot formed by the deflection of relativistic plasma from the primary hotspot. Radio and optical images of 3C 445 South show a spectacular 10-kpc arc-shape structure characterized by two main components, and perpendicular to the jet direction. HST images in I and B bands further resolve the brightest components into thin elongated features. In both 3C 105 South and 3C 445 South the main hotspot components are enshrouded by diffuse optical emission on scale of several kpcs, indicating that very high energy particles, possibly injected at strong shocks, are continuously re-accelerated in situ by additional acceleration mechanisms. We suggest that stochastic processes, linked to turbulence and instabilities, could provide the required additional re-acceleration.

Key words: radio continuum: galaxies - radiation mechanisms: non-thermal - acceleration of particles

1 INTRODUCTION

Radio hotspots are bright and compact regions located at the end of powerful radio galaxies (FRIIs, Fanaroff & Riley 1974) and considered to be the working surfaces of supersonic jets. In these regions, the jet emitted by the active galactic nucleus (AGN) impacts on the surrounding ambient medium producing a shock that may re-accelerate relativistic particles transported by the jet and enhance the radio emission. Electrons responsible for synchrotron emission in the optical band must be very energetic (Lorentz factor $\gamma > 10^5$), and therefore with short radiative lifetime. Consequently the detection of optical emission from

hotspots supports the scenario where the emitting electrons are accelerated at the hotspots, possibly by strong shocks generated by the impact of the jet with the ambient medium (Meisenheimer et al. 1989, 1997; Brunetti et al. 2003). The detection of X-ray synchrotron counterparts of radio hotspots would imply the presence of electrons with even higher energies. However the main radiation process responsible for the X-ray emission seems to differ between high and low luminosity hotspots (Hardcastle et al. 2004). In bright hotspots, like Cygnus A and 3C 295, the X-ray emission is produced by synchrotron-self Compton (SSC) in the presence of a magnetic field that is roughly in equipartition, while in low-luminosity hotspots, like 3C 390.3, the emission at such high energies is likely due to synchrotron radiation (Hardcastle et al. 2007).

The discovery of optical emission extended to kpc scale

---

questions the standard shock acceleration model, suggesting that other efficient mechanisms must take place across the hotspot region. Although it may seem an uncommon phenomenon due to the difficulty to produce high-energy electrons on large scales, deep optical images showed that diffuse optical emission is present in a handful of hotspots: 3C 33, 3C 111, 3C 303, 3C 351 (Lähteenmäki & Valtaoja 1999), 3C 390.3 (Prieto & Kotilainen 1997), 3C 275.1 (Cheung et al. 2005), Pictor A (Thomson et al. 1995), and 3C 445 (Prieto et al. 2002). A possible mechanism able to keep up the optical emission in the post-shock region on kpc scale is a continuous, relatively efficient, stochastic mechanism[1].

The sample of low-power hotspots presented by Mack et al. (2009) is characterized by low magnetic field strengths between 40 and 130 μG, a factor 2 to 5 lower than that estimated in hotspots with optical counterparts previously studied in the literature. A surprisingly high optical detection rate ($\geqslant 45\%$) of the hotspots in this sample was found, and in most cases the optical counterpart extends on kpc scales. This is the case of 3C 445 South, 3C 445 North, 3C 105 South and 3C 227 West (Mack et al. 2009).

This paper focuses on a multi-band, from radio to X-rays, high spatial resolution study of the two most interesting cases among the low-luminosity hotspots from Mack et al. (2009), 3C 105 South and 3C 445 South, in which the hotspot regions are resolved into multiple components. 3C 105 is hosted by a narrow-line radio galaxy (NLRG) at redshift $z = 0.089$ (Tadhunter et al. 1993). At this redshift $1''$ corresponds to 1.642 kpc. The radio source 3C 105 is about $330''$ (542 kpc) in size, and the hotspot complex 3C 105 South is located about $168''$ (276 kpc) from the core in the southeast direction. 3C 445 is hosted by a broad-line radio galaxy (BLRG) at redshift $z = 0.05623$ (Eracleous & Halpern 1994). At this redshift $1''$ corresponds to 1.077 kpc. The radio source 3C 445 is about $562''$ (608 kpc) in size, and the hotspot complex 3C 445 South is located $270''$ (291 kpc) south of the core.

Throughout this paper, we assume the following cosmology: $H_0 = 71$ km/s Mpc^{-1}, $\Omega_M = 0.27$ and $\Omega_\Lambda = 0.73$, in a flat Universe. The spectral index is defined as $S(\nu) \propto \nu^{-\alpha}$.

2   OBSERVATIONS

2.1   Radio observations

VLA observations at 1.4, 4.8, and 8.4 GHz of the radio hotspots 3C 445 South and 3C 105 South were carried out in July 2003 (project code AM772) with the array in A-configuration. Each source was observed for about half an hour at each frequency, spread into a number of scans interspersed with other source/calibrator scans in order to improve the uv-coverage. About 4 minutes were spent on the primary calibrator 3C 286, while secondary phase calibrators were observed for 1.5 min about every 5 min. Data at 1.4 and 4.8 GHz were previously published by

Mack et al. (2009). The data reduction was carried out following the standard procedures for the VLA implemented in the NRAO AIPS package. Final images were produced after a few phase-only self-calibration iterations. The r.m.s. noise level on the image plane is negligible if compared to the uncertainty of the flux density due to amplitude calibration errors that, in this case, are estimated to be $\sim 3\%$.

Besides the *full-resolution* images, we also produced *low-resolution* images at both 4.8 and 8.4 GHz, using the same uv-range, image sampling and restoring beam of the 1.4 GHz data. These new images were obtained with natural grid weighting in order to mitigate the differences in the sampling density at short spacing, and to perform a robust spectral analysis.

2.2   Optical observations

For both 3C 105 South and 3C 445 South, VLT high spatial resolution images in standard filters taken with both ISAAC in J-, H-, K-, and FORS in I-, R-, B- and U- bands are used in this work. All the images have excellent spatial resolutions in the range of $0.5'' < \mathrm{FWHM} < 0.7''$. Details on the observations and data reduction are given in Mack et al. (2009). The pixel scale of the ISAAC images is 0.14 arcsec pixel^{-1}. In the case of the FORS images the pixel scale is 0.2 arcsec pixel^{-1}, with the exception of the I-band where it is 0.1 arcsec pixel^{-1}.

Further HST observations on 3C 445 South only, were obtained with the ACS/HRC camera on 7th July, 2005 in the filters F814W (I-band, exposure time $\sim$ 1.5 hr) and F475W (B-band, exposure time $\sim$ 2.3 hr).

For science analysis we used the "*drz" images delivered by the HST ACS pipeline. These final images are calibrated, cosmic-ray cleaned, geometrically corrected, and drizzle-combined, provided in electrons per sec. The final pixel scale of the drizzled images is $0.025'' \times 0.025''$ per pixel. The flux calibration was done using the standard HST/ACS procedure that relies on the PHOTFLAM keyword in the respective image headers. The quality of the pipeline-delivered images was adequate for the purposes of analyzing the hotspot region.

2.3   X-ray observations

The radio source 3C 105 was observed by *Chandra* on 2007 December 17 (Obs ID 9299) during "The *Chandra* 3C Snapshot Survey for Sources with z<0.3" (Massaro et al. 2010). An $\sim$8 ksec exposure was obtained with the ACIS-S camera, operating in VERY FAINT mode. The data analysis was performed following the standard procedures described in the *Chandra* Interactive Analysis of Observations (CIAO) threads and using the CIAO software package v4.2 (see Massaro et al. 2009 for more details). The *Chandra* Calibration Database (CALDB) version 4.2.2 was used to process all files. Level 2 event files were generated using the *acis_process_events* task, after removing the hot pixels with *acis_run_hotpix*. Events were filtered for grades 0,2,3,4,6, and we removed pixel randomization.

3C 445 South was observed by *Chandra* on 2007 October

---

[1] More recently these stochastic mechanisms have been also proposed for the acceleration of ultra-high energy cosmic-rays in the lobes of radiogalaxies (Hardcastle et al. 2009).

Table 1. Radio flux density and angular size of the hotspot components.
Note 1: deconvolved angular sizes from a Gaussian fit.
Note 2: the angular sizes are derived from the lowest contour on the image plane;
Note 3: The diffuse emission is estimated by subtracting the flux density of SW and SE from the total flux density (see Section 5.3).

Source	Comp.	z	scale kpc/$''$	$S_{1.4}$ mJy	$S_{4.8}$ mJy	$S_{8.4}$ mJy	θ_{maj} arcsec	θ_{min} arcsec
3C 105	S1[1]	0.089	1.642	130±10	67±5	45±5	1.0	0.8
	S2[1]			1250±40	620±20	460±15	1.30	1.0
	S3[1]			1180±35	510±15	320±12	1.5	0.8
	Ext			174±10	75±5	50±3		
3C 445	SE[2]	0.0562	1.077	290±30	98±15	65±10	3.5	1.0
	SW[2]			220±25	51±10	36±6	1.5	0.5
	Diff[3]					13.0±1.1		

18 (Perlman et al. 2010), ACIS chip S3, with an exposure time of 45.6 ksec. The data were retrieved from the archive and analysed following the same procedure as for 3C 105 South. This re-analysis was necessary in order to achieve a proper alignment with the radio data.

We created 3 different flux maps in the soft, medium, and hard X-ray bands (0.5 – 1, 1 – 2, and 2 – 7 keV, respectively) by dividing the data with monochromatic exposure maps with nominal energies = 0.8 keV (soft), 1.4 keV (medium), and 4 keV (hard). Both the exposure maps and the flux maps were regridded to a pixel size of 0.25 the size of a native ACIS pixel (native=$0.492'' \times 0.492''$). To obtain maps with brightness units of ergs cm^{-2} s^{-1} pixel^{-1}, we multiplied each event by the nominal energy of its respective band.

For 3C 445 South, we measured a flux density consistent with what reported by Perlman et al. (2010). The flux density was extracted from *Chandra* ACIS-S images in which the hotspot was placed on axis. Both hotspots have been detected also by *Swift* in the energy range 0.3-10 keV (See Appendix A). This is remarkable given *Swift*'s survey operation mode and its poor spatial resolution. The detection level is about 7σ and 12σ for 3C 105 South and 3C 445 South, respectively. However, given the large *Swift* errors in the counts-to-flux conversion and its low angular resolution, we do not provide any further flux estimate.

2.4 Image registration

The alignment between radio and optical images was done by the superposition of the host galaxies with the nuclear component of the radio source using the AIPS task LGEOM. This results in a shift of $3.5''$. To this purpose, the optical images were previously brought on the same grid, orientation and coordinate system as the radio images by means of the AIPS task CONV and REGR (see also Mack et al. 2009). The final overlay of radio and optical images is accurate to $0.1''$.

For 3C 105 South the X-ray image has been aligned with the radio one by comparing the core position. Then, the final overlay of X-ray contours on the VLT image is accurate to $0.1''$. In the case of 3C 445 the shape of the nucleus of

the galaxy is badly distorted in the *Chandra* image because of its location far off axis of *Chandra*. The alignment was then performed using three background sources visible both in X-ray and B band, and located around the hotspot. The achieved accuracy with this registration is better than 0.15 arcsec, allowing us to confirm a shift of about $2''$ in declination between the X-rays and B-band emission centroids, the X-ray one being the closest to the core (Fig. 2).

3 PHOTOMETRY

To construct the spectral energy distribution (SED) of individual hotspot components, the flux density at the various wavelengths must be accurately measured in the same region, avoiding contamination from unrelated features. To this purpose, we produced a cube where each plane consists of radio and optical images regridded to the same size and smoothed to the same resolution. Then the flux density was derived by means of AIPS task BLSUM which performs an aperture integration on a selected polygonal region common to all the images. The values derived in this way were then used to construct the radio-to-optical SED, and they are reported in Tables 1 and 2.

In addition to the low-resolution approach, we derive the hotspot flux densities and angular sizes on the full resolution images, in order to better describe the source morphology.

On the radio images, we estimate the flux density of each component by means of TVSTAT, which is similar to BLSUM, but instead of working on an image cube it works on a single image. The angular size was derived from the lowest contour on the image plane, and it corresponds to roughly twice the size of the full width half maximum (FWHM) of a conventional Gaussian covering a similar area. In the case of 3C 105 South, the hotspot components are unresolved at 1.4 GHz, and we derive the flux density at this frequency by means of AIPS task JMFIT, which performs a Gaussian fit in the image plane. The angular size was measured on the images in which the components were resolved, i.e. in the case of 3C 105 South we use the 4.8 and 8.4-GHz images, which provide the same value, while for 3C 445 South the components could be reliably resolved

Table 2. Near infrared, optical flux density and X-ray (0.5 - 7 keV) flux of hotspot components. In the case of 3C 445 the X-ray flux is not associated to any of the two main components. The X-ray flux reported refers the total emission measured on the whole hotspot region.
Note 1: units in 10^{-15} erg cm^{-2} s^{-1};
Note 2: the X-ray value, in μJy, is from Perlman et al. (2010);
Note 3: The diffuse emission is inclusive of the SC component and it is estimated by subtracting from the total flux density those arising from SW and SE (see Section 5.3).

Source	Comp.	S_K μJy	S_H μJy	S_J μJy	S_I μJy	S_R μJy	S_B μJy	S_U μJy	S_I^{HST} μJy	S_B^{HST} μJy	S_X
3C 105	S1	4.6±0.9	4.4±1.1	<2.5	-	0.5±0.1	0.2±0.1	-	-	-	7.5±2.4[1]
	S2	18.4±1.4	12.3±1.1	3.4±1.0	-	0.7±0.1	0.2±0.1	-	-	-	<2.0[1]
	S3	31.9±2.8	25.7±2.9	4.4±1.8	-	0.9±0.1	0.3±0.1	-	-	-	3.2±1.6[1]
	Ext	15.4±2.0	5.4±2.0	-	-	0.4±0.1	0.2±0.1	-	-	-	-
3C 445	SE	8.0±1.0	5.6±2.0	6.0±1.5	2.0±0.2	1.3±0.2	0.7±0.1	0.5±0.3	1.7±0.2	1.5±0.3	9.38×10^{-4} [2]
	SW	4.6±1.4	3.6±1.5	3.0±0.4	1.7±0.3	1.4±0.1	0.7±0.1	0.5±0.2	1.4±0.1	0.3±0.1	-
	SC	-	-	-	-	0.8±0.1	0.6±0.1	0.4±0.1	-	-	-
	Diff[3]	-	2.1±0.6	3.2±1.3	1.2±0.2	1.0±0.2	0.8±0.2	-			

in the image at 8.4 GHz only (Table 1).

Full-resolution infrared and optical flux densities of hotspot sub-components were measured by means of the IDL-based task ATV using a circular aperture centred on each component. Such values were compared to those derived from the analysis of the cube and they were found to be within the expected uncertainties.

For the X-ray flux we constructed photometric apertures to accommodate the *Chandra* point spread function and to include the total extent of the radio structures. The background regions, with a total area typically twice that of the source region, have been selected close to the source, and centred on a position where other sources or extended structures are not present. The X-ray flux was measured in any aperture with only a small correction for the ratio of the mean energy of the counts within the aperture to the nominal energy for the band. We note that in 3C 105 South, the hotspot components are well separated ($2''$), allowing us to accurately isolate the corresponding X-ray emission. In 3C 445 South the X-ray emission is not associated with the two main components clearly visible in the radio and optical bands, and flux was derived by using an aperture large enough to include all of the X-ray emission extending over the entire hotspot region. Our estimated value is in agreement with the one reported by Perlman et al. (2010). All X-ray flux densities have been corrected for the Galactic absorption with the column density $N_H = 1.15 \cdot 10^{21}$ cm^{-2} given by Kalberla et al. (2005). X-ray fluxes are reported in Table 2.

4   MORPHOLOGY

4.1   3C 105 South

The southern hotspot complex of 3C 105 shows a curved structure of about $8'' \times 4.5''$ ($\sim 13 \times 7$ kpc) in size. It is dominated by three bright components, all resolved at radio frequencies, connected by a low surface brightness emission also visible in optical and infrared (Fig. 1). The central component, labeled S2 in Fig. 1, is the brightest in radio and, when imaged with high spatial resolution, it is resolved in two different structures separated by about 1.2 kpc. Leahy et al. (1997) interpreted this as the true jet termination hotspot, while S1, with an elongated structure of (1.6×1.3) kpc and located 5.7 kpc to the north of S2 is considered as jet emission. The southernmost component S3, located about 4.1 kpc from S2, has a resolved structure of (2.4×1.3) kpc in size, and it is elongated in a direction perpendicular to the line leading to S2. Its morphology suggests that S3 is a secondary hotspot similar to 3C 20 East (Cox et al. 1991).

At 1.4 GHz, an extended tail accounting for $S_{1.4} = 608$ mJy and embedding the jet is present to the west of the hotspot complex, in agreement with the structure previously found by Neff et al. (1995). At higher frequencies the lack of the short spacings prevents the detection of such an extended structure, and only a hint of the jet, accounting for $S_{4.8} \sim 70$ mJy, is still visible at 4.8 GHz.

In the optical and NIR the hotspot complex is characterized by the three main components detected in radio. In NIR and optical, the southernmost component S3 is the brightest one, with a radio-to-optical spectral index $\alpha_{r-o} = 0.95 \pm 0.10$. It displays an elongated structure rather similar in shape and size to that found in radio. It is resolved in all bands with the only exception of B band, likely due to the lower spatial resolution achieved. Component S1 is resolved in all NIR/optical bands, showing a tail extending towards S2. Its radio-to-optical spectral index is $\alpha_{r-o} = 0.95 \pm 0.10$. On the other hand, S2 appears unresolved in all bands, with the exception of K and H bands, i.e. those with the highest resolution achieved. In these NIR bands S2 is extended in the southern direction, resembling what is observed in radio. Its radio-to-optical spectral index is $\alpha_{r-o} = 1.05 \pm 0.10$.

Diffuse emission connecting the main hotspot components and extending to the southwestern part of the hotspot complex is detected in most of the NIR and optical images.

In the X-ray band, S1 is the brightest component, whereas the emission from S3 is very weak (formally detected at only 2σ level). For this reason in the following we will use the
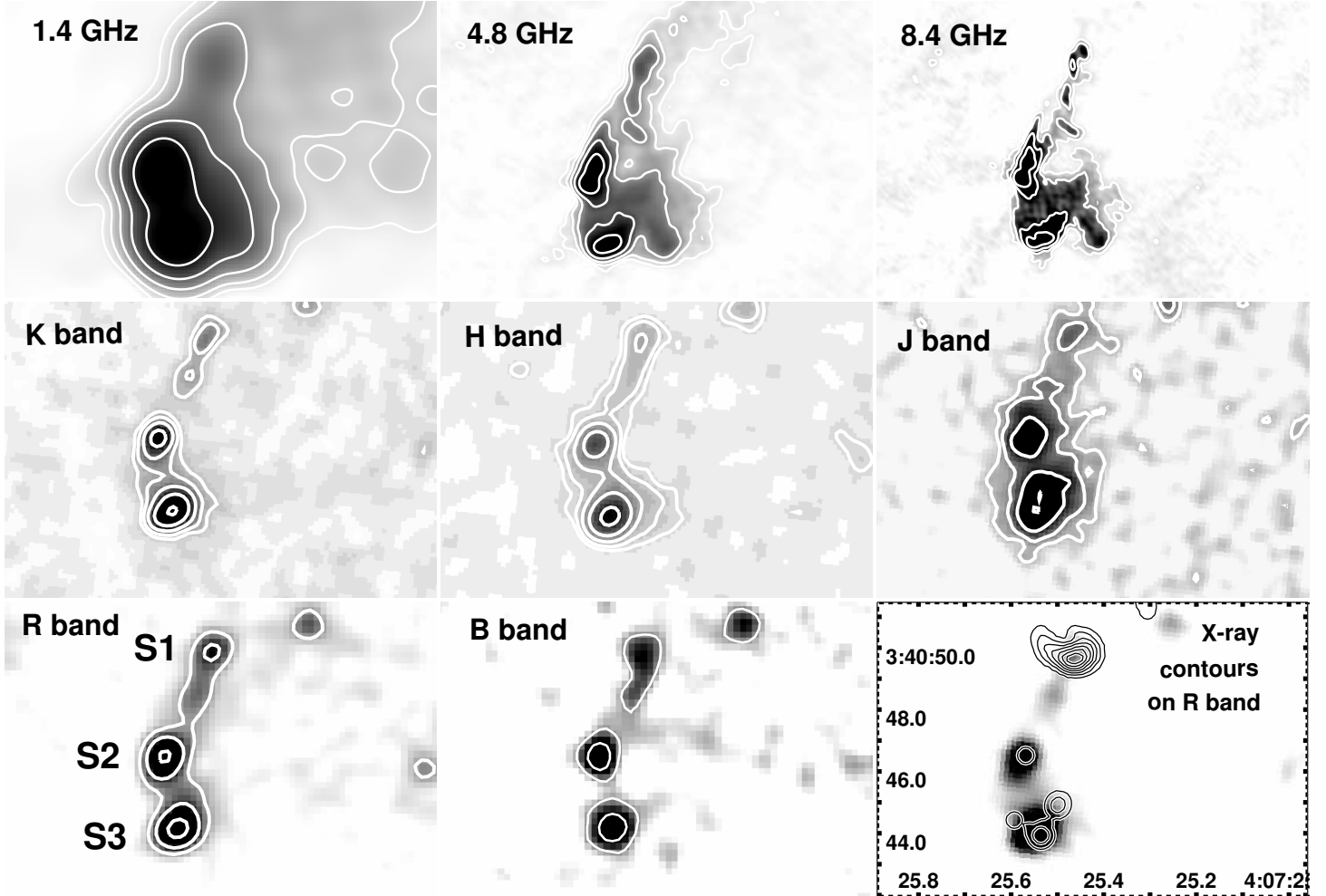
Figure 1. Multifrequency images of 3C 105 South. From the left to right and top to bottom: Radio images at 1.4, 4.8, 8.4 GHz (VLA A-array), NIR/optical images in K, H, J, R, B bands (VLT), and X-ray 0.5-7 keV (*Chandra*) contours. Each panel covers 9.5″ (15.6 kpc) in DEC and 14″ (23 kpc) in RA. In the radio images the lowest contours are 0.9 mJy/beam at 1.4 GHz, 0.20 mJy/beam at 4.8 GHz, and 0.18 mJy/beam at 8.4 GHz, and they correspond to 3 times the off-source rms noise level measured on the image plane. Contours increase by a factor of 4. The restoring beam is 1.3″×1.1″ at 1.4 GHz, 0.38″×0.36″ at 4.8 GHz, and 0.32″×0.22″ at 8.4 GHz. In the optical images the contour levels are in arbitrary units and increase by a factor of 2. The FWHM is about 0.4″, 0.5″, 0.7″, 0.6″, 0.7″ in K, H, J, R, and B band respectively. The X-ray contours were generated from an 0.5-7 keV image, smoothed with a Gaussian of FWHM=0.72″. Contour levels increase linearly: 0.02, 0.04, 0.06,.. 0.14 counts per 0.123″ pixel. The X-ray contours are superposed to the R band image, previously shifted as so to align with X-ray.

nominal X-ray flux of S3 as a conservative upper limit. For component S2 only an upper limit could be set.

4.2   3C 445 South

The hotspot 3C 445 South displays an extended east-west structure of about 9.3″ × 2.8″ (10×3 kpc) in size in radio (Fig. 2). At 8.4 GHz, the hotspot complex is almost com-

pletely resolved out and the two main components, clearly visible in NIR/optical images, are hardly distinguishable. When imaged with enough resolution, these components display an arc-shaped structure both in radio and NIR/optical bands, with sizes of about (3.4×1.5) kpc and (2.1×1.1) kpc for SE and SW respectively. Component SE is elongated in a direction almost perpendicular to the line leading to the source core, while SW forms an angle of about -20° with the same line.
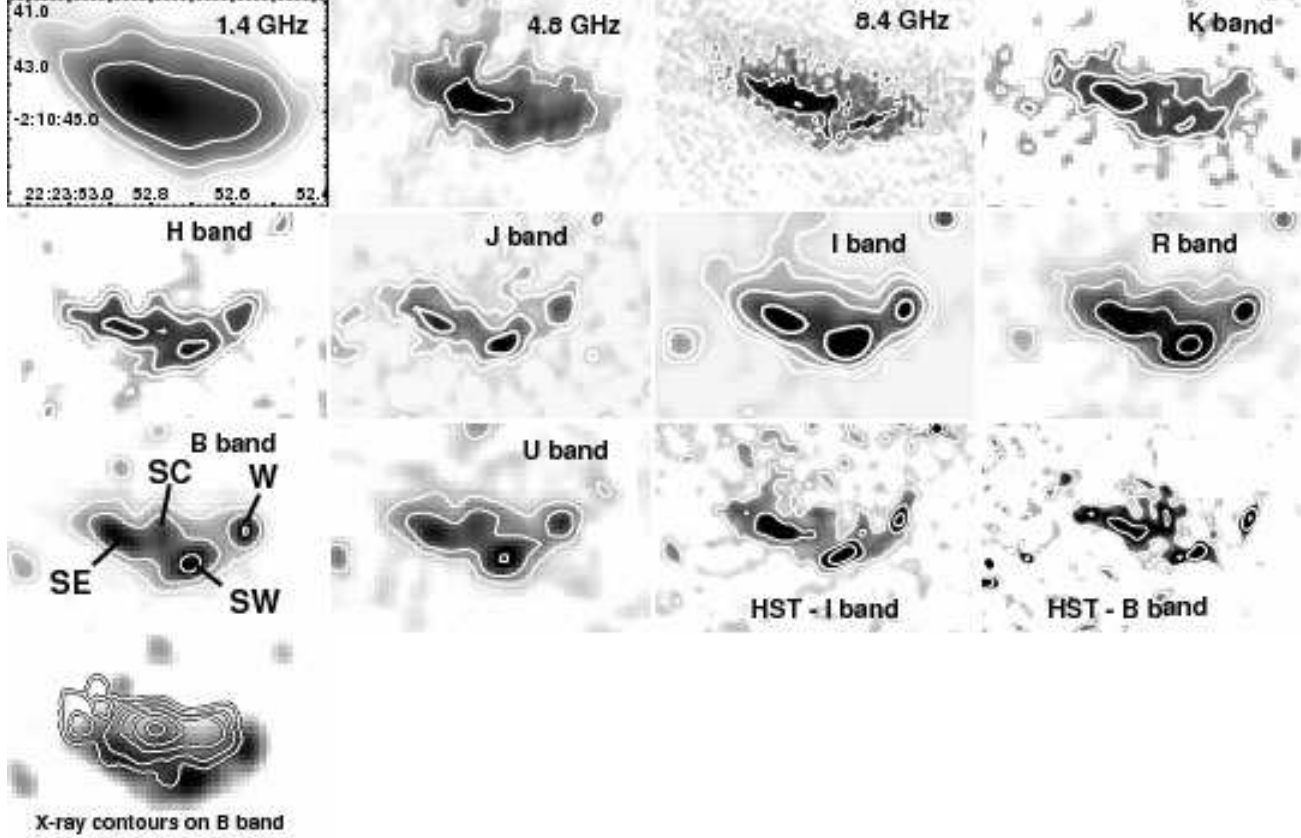
Figure 2. Multifrequency images of 3C 445 South. From the left to right and top to bottom: Radio images at 1.4, 4.8, 8.4 GHz (VLA A-array), NIR/optical images in K, H, J, I, R, B, U bands (VLT), optical images in I and U bands (HST), and X-ray 0.5-7 keV (*Chandra*) contours. Each panel covers 7.3″ (7.8 kpc) in DEC and 11.4″ (12.2 kpc) in RA. In the radio images the lowest contours are 1.3 mJy/beam at 1.4 GHz, 0.20 mJy/beam at 4.8 GHz, and 0.10 mJy/beam at 8.4 GHz, and they correspond to 3 times the off-source rms noise level measured on the image plane. Contours increase by a factor of 4. The restoring beam is 1.43″×0.96″ at 1.4 GHz, 0.45″×0.37″ at 4.8 GHz, and 0.24″×0.21″ at 8.4 GHz. In the optical images the contour levels are in arbitrary units and increase by a factor of 2. The VLT FWHM are 0.7″, 0.6″, 0.5″, 0.7″, 0.6″, 0.6″, 0.7″, in K, H, J, I, R, B, and U band respectively. In HST images each pixel is 0.025″. The X-ray contours in the last panel are superposed on the B band image. They come from an 0.5-7 keV image, smoothed with a Gaussian of FWHM=0.87″. Contour levels increase by a factor of 2; the lowest contour is at a brightness of 0.01 counts per 0.0615″ pixel.

In radio and NIR, the SE component is the brightest one, with a flux density ratio SE/SW $\sim$ 1.6, while in the optical both components have similar flux densities. Both components have a radio-to-optical spectral index $\alpha_{r-o} = 0.9 \pm 0.10$. In the optical R-, B-, and U-band images a third component (labelled SC in Fig. 2) aligned with the jet direction becomes visible between SE and SW. Despite the good resolution and sensitivity of the radio and NIR images, SC is not present at such wavelengths. When imaged with the high resolution provided by HST, both SE and SW are clearly resolved, and no compact regions can be identi-

fied in the hotspot complex. Trace of the SC component is seen in the B-band, in agreement with the VLT images.

In the VLA and VLT images, the two main components are enshrouded by a diffuse emission, visible in radio and NIR/optical bands. The flux densities of the SE and SW components measured on the HST images are consistent (within the errors) with those derived on the VLT images. The optical component W located about 2.8″ (3 kpc) on the northwestern part of SW does not have a radio counterpart, as it is clearly shown by the superposition of I-band HST and 8.4-GHz VLA images (Fig. 3), and thus it is considered
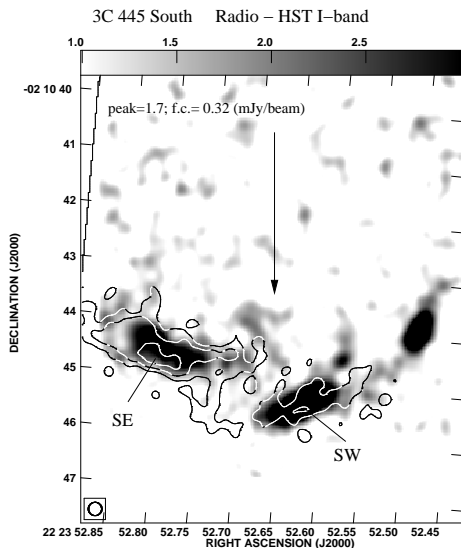
Figure 3. 3C 445 South. 8.4-GHz VLA contours are superimposed on the I-band HST image.

an unrelated object, like a background galaxy. Another possibility is that this is a synchrotron emitting region where the impact of the jet produces very efficient particle acceleration. However, its steep optical spectrum ($\alpha \sim 2$ between I and U bands, see Section 5.3, Fig. 10) together with the absence of detected radio emission disfavour this possibility. Future spectroscopic information would further unveil the nature of this optical region.

Chandra observations of 3C 445 South detected X-ray emission from a region that extends over $6''$ in the east-west direction (Fig. 2), and it peaks almost in the middle of the hotspot structure, suggesting a spatial displacement between X-ray and radio/NIR/optical emission (Perlman et al. 2010).

5   SPECTRAL ENERGY DISTRIBUTION

5.1   The broad-band energy distribution

We model the broad band energy distribution, from radio to optical, of the hotspot regions in order to determine the mechanisms at the basis of the emission. The comparison between the model expectation in the X-rays and *Chandra* data sets additional constraints. In the adopted models, the hotspot components are described by homogeneous spheres with constant magnetic field and constant properties of the relativistic electron populations. The spectral energy distributions of the emitting electrons are modelled assuming the formalism described in Brunetti et al. (2002). According to this model a population of seed electrons (with $\gamma \leqslant \gamma_*$) is accelerated at the shock and is injected in the downstream region with a spectrum $\mathrm{dN}(\gamma)/\mathrm{dt} \propto \gamma^{-p}$, for $\gamma_* < \gamma < \gamma_c$, γ_c being the maximum energy of the electrons accelerated at the shock. Electrons accelerated at the shock are advected in the downstream region and age due to radiative losses.
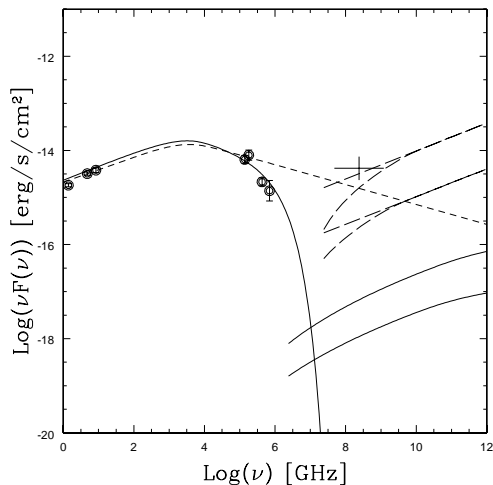

Figure 4. The broad-band SED of the northern component, S1, of 3C 105 South. The solid lines represent the synchrotron model where $\nu_{\mathrm{b}} = 5 \times 10^{12}$ Hz and $\nu_{\mathrm{c}} = 2 \times 10^{15}$ Hz, and the SSC models computed assuming a magnetic field of 50 and 150 μG. The short-dashed line represent a synchrotron model where $\nu_{\mathrm{b}} = 5 \times 10^{12}$ Hz, and $\nu_{\mathrm{c}} = \infty$. The long-dashed lines represent the IC-CMB models computed assuming B=16 (and B=32) μG, Γ=6 ($\Gamma = 4$), θ=0.1 ($\theta = 0.2$) rad, with or without flattening in the observed synchrotron spectrum at $\nu < 60$ MHz. The magnetic field is in the rest frame.
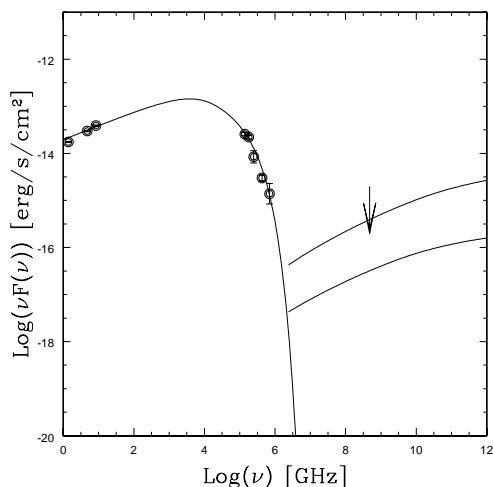

Figure 5. The broad-band SED of the central component, S2, of 3C 105 South. The solid line represents the synchrotron model where $\nu_{\mathrm{b}} = 7.5 \times 10^{12}$ Hz and $\nu_{\mathrm{c}} = 3 \times 10^{14}$ Hz, and the SSC models computed assuming a magnetic field of 50 and 225 μG. The arrow indicates the X-ray upper limit.

Based on Brunetti et al. (2002), the volume integrated spectrum of the electron population in the downstream region of size $L \sim T v_{\mathrm{adv}}$ (T and v_{adv} being the age and the advection velocity of the downstream region) is given by either a steep power-law $N(\gamma) \propto \gamma^{-(p+1)}$ for $\gamma_b < \gamma < \gamma_c$, where γ_b is the maximum energy of the "oldest" electrons in the downstream region, or by $N(\gamma) \propto \gamma^{-p}$ for $\gamma_* < \gamma < \gamma_b$, or by a flatter shape for $\gamma_{\mathrm{low}} < \gamma < \gamma_*$, where γ_{low} is the
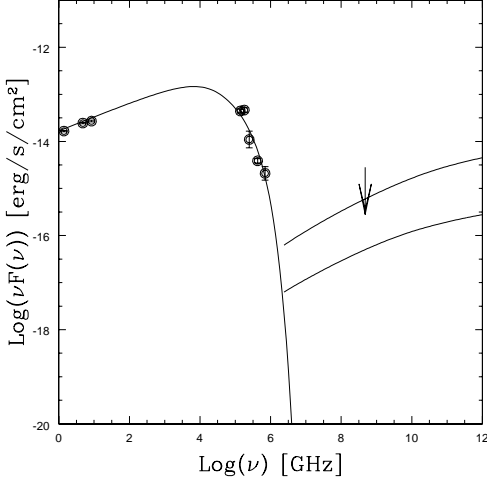
Figure 6. The broad-band SED of the southern component, S3, of 3C 105 South. The solid line represents the synchrotron model where $\nu_{\rm b} = 1.5 \times 10^{13}$ Hz and $\nu_{\rm c} = 3 \times 10^{14}$ Hz, and the SSC models computed assuming a magnetic field of 50 and 150 μG. The arrow indicates the X-ray upper limit.
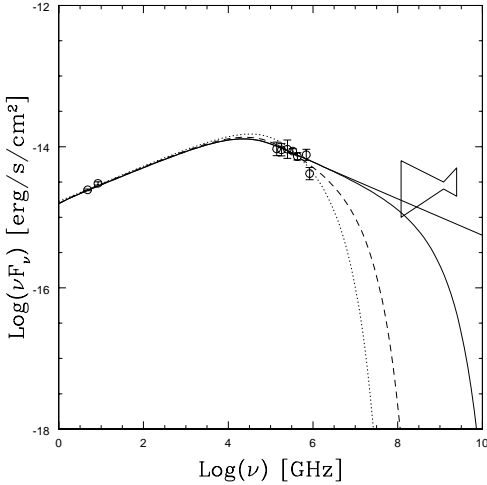

Figure 8. The broad-band SED of the eastern component, SE, of 3C 445 South. The morphology from *Chandra* image shows that X-rays are not associated with the eastern component. The synchrotron models assume $\nu_{\rm b} = 5.2 \times 10^{13}$ Hz and $\nu_{\rm c} = 2.6 \times 10^{15}$ Hz (*dotted line*), $\nu_{\rm b} = 2.4 \times 10^{13}$ Hz and $\nu_{\rm c} = 9.4 \times 10^{15}$ Hz (*dashed line*), $\nu_{\rm b} = 1.2 \times 10^{13}$ Hz and $\nu_{\rm c} = 4.7 \times 10^{17}$ Hz (*solid line*), $\nu_{\rm b} = 1.2 \times 10^{13}$ Hz and $\nu_{\rm c} = \infty$ (*thick solid line*).
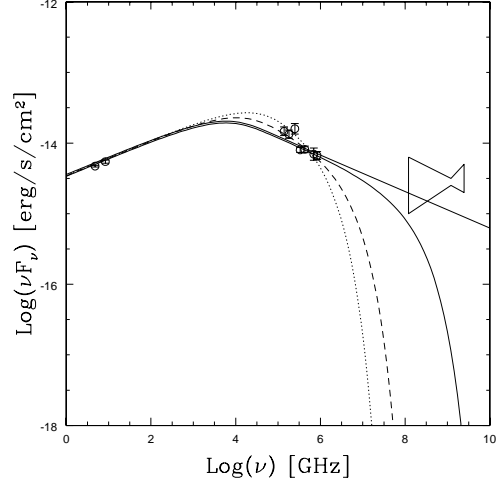

Figure 7. The broad-band SED of the western component, SW, of 3C 445 South. The morphology from *Chandra* image shows that X-rays are not associated with the western component. The synchrotron models assume $\nu_{\rm b} = 9.4 \times 10^{13}$ Hz and $\nu_{\rm c} = 4.7 \times 10^{15}$ Hz (*dotted line*), $\nu_{\rm b} = 5.5 \times 10^{13}$ Hz and $\nu_{\rm c} = 2.2 \times 10^{16}$ Hz (*dashed line*), $\nu_{\rm b} = 4.4 \times 10^{13}$ Hz and $\nu_{\rm c} = 1.8 \times 10^{18}$ Hz (*solid line*), $\nu_{\rm b} = 4.4 \times 10^{13}$ Hz and $\nu_{\rm c} = \infty$ (*thick solid line*).
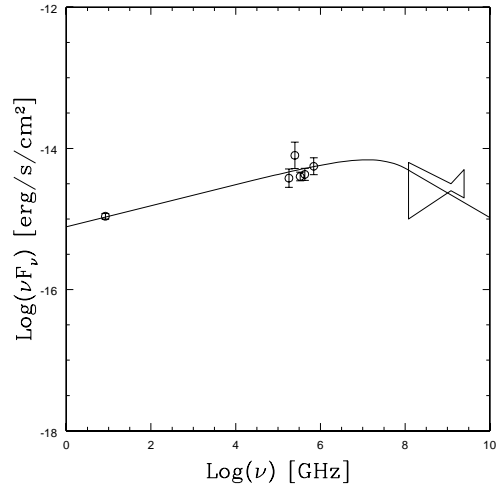

Figure 9. The broad-band SED of the diffuse emission (see text) of 3C 445 South. The morphology from the *Chandra* image does not allow us to firmly exclude a connection between the X-rays and the diffuse (including SC component) emission. The synchrotron model assumes $\nu_{\rm b} = 8 \times 10^{16}$ Hz, $\nu_{\rm c} \gg \nu_{\rm b}$ and p=2.7.

minimum energy of electrons accelerated at the shock.
As the first step we fit the SED in the radio-NIR-optical regimes with a synchrotron model, and we derive the relevant parameters of the synchrotron spectrum (injection spectrum α, break frequency $\nu_{\rm b}$, cut-off frequency $\nu_{\rm c}$) and the slope of the energy distribution of the electron population as injected at the shock (p $= 2\alpha + 1$). Since hotspots have spectra with injection slope α ranging between 0.5 and 1 (as a reference, the classical value

from the diffuse particle acceleration at strong shocks is $\alpha = 0.5$, e.g. Meisenheimer et al. 1997), we decided to consider the injection spectral index as a free parameter. Such constraints allow us to determine the spectrum of the emitting electrons (normalization, break and cut-off energy), once the magnetic field strength has been assumed, and to calculate the emission from either synchrotron-self-Compton (SSC) or inverse-Compton scattering of the

Table 3. Synchrotron parameters. Column 1: Hotspot; Column 2: component; Columns 3, 4: spectral index and break frequency as derived from the fit to the radio-to-optical SED (Section 5.1); Column 5: equipartition magnetic field, computed following the approach presented in Brunetti et al. (2002); Column 6: radiative age computed using Eq. 2.

Source	Comp.	α	$\nu_{\rm b}$ 10^{13} Hz	$B_{\rm eq}$ μG	$t_{\rm rad}$ yr
3C 105	S1	0.8	0.50	150	12
	S2	0.8	0.75	290	4
	S3	0.8	1.5	270	3
3C 445	SE	0.75	5.2	60	15
	SW	0.75	9.4	50	15

cosmic background radiation (IC-CMB) expected from the hotspot (or jet) region (following Brunetti et al. 2002). Models described in Brunetti et al. (2002) take also into account the boosting effects arising from a hotspot/jet that is moving at relativistic speeds and oriented at a given angle with respect to our line of sight.

5.2 3C 105 South

In Figures 4 to 6 we show the SED from the radio band to high energy emission measured for the hotspot components of 3C 105 South, together with the model fits. Synchrotron models with an injection spectral index α=0.8 provide an adequate representation of the SED of the central and southern components of 3C 105 South, with break frequencies ranging from 5×10^{12} to 1.5×10^{13} W/Hz, while the cutoff frequencies are between 3×10^{14} and 2×10^{15} W/Hz. In both components, the upper limit to the X-ray emission does not allow us to constrain the validity of the SSC model (Figs. 5 and 6). On the other hand, the northern component of 3C 105 shows a prominent X-ray emission. A synchrotron model (dashed line in Fig. 4) may fit quite reasonably the radio, NIR and X-ray emission, but it completely fails in reproducing the optical data. An additional contribution of the SSC is not a viable option since it requires a magnetic field much smaller than that obtained assuming equipartition (see Section 5.4) (solid lines), and implying an unreasonably large energy budget. On the other hand, the high energy emission is well modelled by IC-CMB (e.g. Tavecchio et al. 2000; Celotti et al. 2001) where the CMB photons are scattered by relativistic electrons with Lorentz factor $\Gamma \sim 6$, and θ=5° with a magnetic field of 16 μG. This model implies that boosting effects play an important role in the X-ray emission of this component, suggesting that S1 is more likely a relativistic knot in the jet, rather than a hotspot feature. The weakness of this interpretation is that 3C 105 is a NLRG and its jets are expected to form a large angle with our line of sight. Alternatively, the X-ray emission may be synchrotron from a different population of electrons, as suggested in the case of the jet in 3C 273 (Jester et al. 2007).

5.3 3C 445 South

The analysis of the southern hotspot of 3C 445 as a single unresolved component was carried out in previous work by Prieto et al. (2002); Mack et al. (2009); Perlman et al. (2010). In this new analysis, the high spatial resolution and multiwavelength VLT and HST data of 3C 445 South allow us to study the SED of each component separately in order to investigate in more detail the mechanisms at work across the hotspot region. In Figures 7 to 9 we show the SED from the radio band to high energy emission measured for the components of 3C 445 South, together with the model fits. We must note that at 1.4 GHz the resolution is not sufficient to reliably separate the contribution from the two main components. For this reason, we do not consider the flux density at this frequency in constructing the SED. The X-ray emission (Fig. 2) is misaligned with respect to the radio-NIR-optical position. For this reason, on the SED of both components (Figs. 7 and 8) we plot the total X-ray flux which must be considered an upper limit. For the components of 3C 445 South the synchrotron models with α=0.75 reasonably fit the data, providing break frequencies in the range of 10^{13} and 10^{14} W/Hz, and cutoff frequencies from 10^{15} Hz and 10^{18} Hz.

Both the morphology (Fig. 2) and the SED (Figs. 7 and 8) indicate that the bulk of *Chandra* X-ray emission detected in 3C 445 is not due to synchrotron emission from the two components (Section 6).

As discussed in Section 4.2, diffuse IR and optical emission surrounds the two components SE and SW of 3C 445 South, and a third component, SC, becomes apparent in the optical. We attempt to evaluate the spectral properties of the diffuse emission (including component SC). When possible, depending on statistics, we subtract from the total flux density of the hotspot, the contribution arising from the two main components, obtaining in this way the SED of the diffuse emission (inclusive of SC component) of 3C 445 South. In the image we also plot the total X-ray flux. As expected the emission has a hard spectrum ($\alpha \sim 0.85$) without evidence of a break up to the optical band, 10^{15} Hz $< \nu_b \leqslant 8 \times 10^{16}$ Hz. We also note that this hard component may represent a significant contribution of the observed X-ray emission, although the X-ray peak appears shifted ($\sim 1''$) from the SC component. Due to the extended nature of the emission in this hotspot, we created a power-law spectral index map illustrating the change of the spectral index α across the hotspot region (Fig. 10). The spectral energy distributions presented in Figs. 7, 8, and 9 show the curvature of the integrated spectrum for the main components and the diffuse emission (see Section 5.1). The spectral map in Fig. 10 attempts to provide complementary information on the spectral slope for the diffuse inter-knot emission. Extracting these maps using the largest possible frequency range is complicated as it implies combining images from different instruments with different scale sampling, noise pattern, etc. These effects sum up to produce very low contrast maps given the weakness of the hotspot signal. To minimise these effects it was decided to extract the slope maps from the optical and -IR images only.

The spectral index map between I- and U-band (Fig. 10) shows two sharp edges, at the SW and SE components,

with the highest value $\alpha \sim 1.5$. Between these two main regions there is diffuse emission that is clearly seen in the I-/U-band spectral index map. The slope of this component is flatter than that of the two main regions and rather uniform all over the hotspot, with $\alpha \sim 1$.

5.4 Physical parameters

We compute the magnetic field of each hotspot component by assuming minimum energy conditions, corresponding to equipartition of energy between radiating particles and magnetic field, and following the approach by Brunetti et al. (1997). We assume for the hotspot components an ellipsoidal volume V with a filling factor $\phi=1$ (i.e. the volume is fully and homogeneously filled by relativistic plasma). The volume V is computed by means:

$$V = \frac{\pi}{6} d_{\min}^2 d_{\max} \qquad (1)$$

where $d_{\min}$ and $d_{\max}$ are the linear size of the minor and major axis, respectively. We consider $\gamma_{\min} = 100$, and we assume that the energy densities of protons and electrons are equal. We find equipartition magnetic fields ranging from $\sim 50 - 290$ μG (Table 3) that is lower than those inferred in high-power radio hotspots which range from ~ 250 to 650 μG (Meisenheimer et al. 1997; Cheung et al. 2005). Remarkably, if we compare these results with those from Mack et al. (2009), we see that in 3C 445 South the value computed considering the entire source volume is similar to those obtained in its individual sub-components, suggesting that compact and well-separated emitting regions are not present in the hotspot volume. On the other hand, the magnetic field averaged over the whole 3C 105 South hotspot complex is much smaller than those derived in its sub-components.

In the presence of such low magnetic fields high-energy electrons may have longer radiative lifetime than in high-power radio hotspots. The radiative age $t_{\rm rad}$ is related to the magnetic field and the break frequency by[2]:

$$t_{\rm rad} = 1610 \, B^{-3/2} \nu_b^{-1/2} (1+z)^{-1/2} \qquad (2)$$

where B is in μG, ν_b in GHz and $t_{\rm rad}$ in 10^3 yr. If in Eq. 2 we assume the equipartition magnetic field we find that the radiative ages are just a few years (Table 3). As the hotspots extend over kpc distances, it is indicative that a very efficient re-acceleration mechanism is operating in a similar way over the entire hotspot region.

6   DISCUSSION

The detection of diffuse optical emission occurring well outside the main shock region and distributed over a

---

[2] The magnetic field energy density in these hotspots are at least an order of magnitude higher than the energy density of the cosmic microwave background (CMB) radiation. Inverse Compton losses due to scattering of CMB photons are negligible.
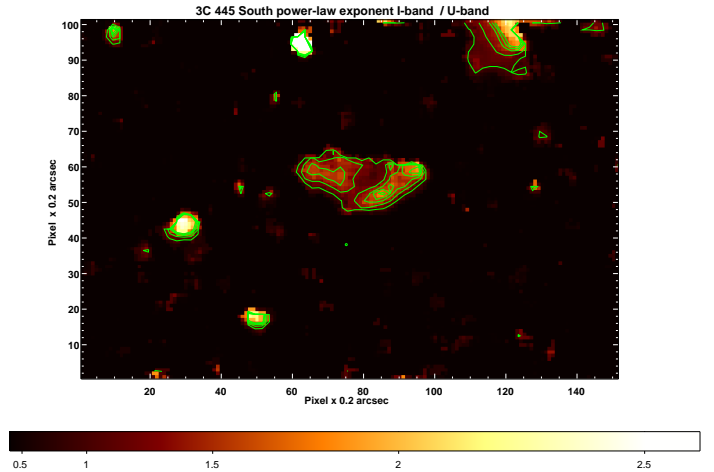

Figure 10. Power-law spectral index map for 3C 445 South determined from FORS I-band and FORS U-band. Contours are 1, 1.3, 1.5, 1.6, 1.7. First contour is 3 sigma.

large fraction of the whole kpc-scale hotspot structure is somewhat surprising. Deep optical observations pointed out that this is a rather common phenomenon detected in about a dozen hotspots (e.g. Mack et al. 2009; Cheung et al. 2005; Thomson et al. 1995). First-order Fermi acceleration alone cannot explain optical emission extending on kpc scale and additional efficient mechanisms taking place away from the main shock region should be considered, unless projection effects play an important role in smearing compact regions where acceleration is still occurring.

Theoretically, we can consider several scenarios that are able to reproduce the observed extended structures. (1) One possibility is that a very wide jet, with a size comparable to the hotspot region, impacts simultaneously into various locations across the hotspot generating a complex shocked region that defines an arc-shaped structure. This, combined with projection effects may explain a wide (projected) emitting region. (2) Another possibility is a narrow jet that impacts into the hotspot in a small region where electrons are accelerated at a strong shock. In this case the accelerated particles are then transported upstream in the hotspot volume where they are continuously re-accelerated by stochastic mechanisms, likely due to turbulence generated by the jet and shock itself. (3) Finally, extended emission may be explained by the "dentist's drill" scenario, in which the jet impacts into the hotspot region in different locations at different times.

The peculiar morphology and the rather high NIR/optical luminosity of 3C 105 South and 3C 445 South, makes these hotspots ideal targets to investigate the nature of extended diffuse emission.

In 3C 105 South, the detection of optical emission in both primary and secondary hotspots implies that in these regions there is a continuous re-acceleration of particles. The secondary hotspot S3 could be interpreted as a splatter-spot from material accelerated in the primary one, S2 (Williams & Gull 1985). Both the alignment and the distance between these components exclude the jet drilling scenario: the light time between the two components is

more than 10^4 years, i.e. much longer than their radiative time (Table 3), suggesting that acceleration is taking place in both S2 and S3 simultaneously. The secondary hotspot S3 shows some elongation, always in the same direction, in all the radio and optical images with adequate spatial resolution. This elongation is expected in a splatter-spot and it follows the structure of the shock generated by the impact of the outflow from the primary upon the cocoon wall.

This scenario, able to explain the presence of optical emission from two bright and distant components, fails in reproducing the diffuse optical emission enshrouding the main features, and the extended tail. In this case, an additional contribution from stochastic mechanisms caused by turbulence in the downstream region is necessary. Although this acceleration mechanism is in general less efficient than Fermi-I processes, the (radiative) energy losses of particles are smaller in the presence of low magnetic fields, such as those in between S2 and S3, (potentially) allowing stochastic mechanisms to maintain electrons at high energies.

In 3C 445 South the observational picture is complex. The optical images of 3C 445 South show a spectacular 10-kpc arc-shape structure. High resolution HST images allow a further step since they resolve this structure in two elongated components enshrouded by diffuse emission. These components may mark the regions where a "dentist's drill" jet impacts on the ambient medium, representing the most recent episode of shock acceleration due to the jet impact. On the other hand, they could simply trace the locations of higher particle-acceleration efficiency from a wide/complex interaction between the jet and the ambient medium. However, the transverse extension, about 1 kpc, of the two elongated components is much larger than what is derived if the relativistic particles, accelerated at the shock, age in the downstream region (provided that the hotspot advances at typical speeds of 0.05-0.1c). Furthermore, the diffuse optical emission on larger scale suggests the presence of additional, complex, acceleration mechanisms, such as stochastic processes, able to keep particle re-acceleration ongoing in the hotspot region. The detection of X-ray emission with *Chandra* adds a new grade of complexity. This emission and its displacement are interpreted by Perlman et al. (2010) as due to IC-CMB originating in the fast part of the decelerating flow. Their model requires that the angle between the jet velocity and the observer's line of sight is small. However, 3C 445 is a classical double radio galaxy and the jet should form a large angle with the line of sight (see also Perlman et al. 2010). On the other hand, we suggest that the X-ray/optical offset might be the outcome of ongoing efficient particle acceleration occurring in the hotspot region. An evidence supporting this interpretation may reside on the faint and diffuse blob seen in U- and B-bands (labelled SC in Fig. 2) just about $1''$ downstream the X-ray peak. The surface brightness of this component decreases rapidly as the frequency decreases, as it is shown in Fig. 2: well-detected in U- and B-bands, marginally visible in I-band, and absent at NIR and radio wavelengths. The SED of the diffuse hotspot emission (including SC component and excluding SW and SE) is consistent with synchrotron emission with a break at high frequencies, 10^{15} Hz $< \nu_b \leqslant 8 \times 10^{16}$ Hz, and may significantly contribute to the observed X-ray flux. Such a hard spectrum is in agreement with (i) a very recent episode of particle acceleration (the radiative cooling time of the emitting particles being 10^2-10^3 yr); (ii) efficient spatially-distributed acceleration processes, similar to the scenario proposed for the western hotspot of Pictor A (Tingay et al. 2008, see their Fig.5).

7 CONCLUSIONS

We presented a multi-band, high spatial resolution study of the hotspot regions in two nearby radio galaxies, namely 3C 105 South and 3C 445 South, on the basis of radio VLA, NIR/optical VLT and HST, and X-ray *Chandra* observations. At the sub-arcsec resolution achieved at radio and optical wavelengths, both hotspots display multiple resolved components connected by diffuse emission detected also in optical. The hotspot region in 3C 105 resolves in three major components: a primary hotspot, unresolved and aligned with the jet direction, and a secondary hotspot, elongated in shape, and interpreted as a splatter-spot arising from continuous outflow of particles from the primary. Such a feature, together with the extremely short radiative ages of the electron populations emitting in the optical, indicates that the jet has been impacting almost in the same position for a long period, making the drilling jet scenario unrealistic. The detection of an excess of X-ray emission from the northern component of 3C 105 South suggests that this region is likely a relativistic knot in the jet rather than a genuine hotspot feature. The optical diffuse emission enshrouding the main components and extending towards the tail can be explained possibly assuming additional stochastic mechanisms taking place across the whole hotspot region.

In the case of 3C 445 South the optical observations probe a scenario where the interaction between jet and the ambient medium is very complex. Two optical components pinpointed by HST observations mark either the locations where particle acceleration is most efficient or the remnants of the most recent episodes of acceleration. Although projection effects may play an important role, the morphology and the spatial extension of the diffuse optical emission suggest that particle accelerations, such as stochastic mechanisms, add to the standard shock acceleration in the hotspot region. The X-rays detected by *Chandra* cannot be the counterpart at higher energies of the two main components. It might be due to IC-CMB from the fast part of a decelerating flow. Alternatively the X-rays could pinpoint synchrotron emission from recent episodes of efficient particle acceleration occurring in the whole hotspot region, similarly to what proposed in other hotspots, that would make the scenario even more complex. A possible evidence supporting this scenario comes from the hard spectrum of the diffuse hotspot emission and from the appearance of a new component (SC) in the optical images.

for the grant awarded him in 2010 to support his research. The VLA is operated by the US National Radio Astronomy Observatory which is a facility of the National Science Foundation operated under cooperative agreement by Associated Universities, Inc. This work has made use of the NASA/IPAC Extragalactic Database NED which is operated by the JPL, Californian Institute of Technology, under contract with the National Aeronautics and Space Administration. This research has made used of SAOImage DS9, developed by the Smithsonian Astrophysical Observatory (SAO). Part of this work is based on archival data, software or on-line services provided by ASI Science Data Center (ASDC). The work at SAO is supported by supported by NASA-GRANT GO8-9114A. We acknowledge the use of public data from the Swift data archive. This research has made use of software provided by the Chandra X-ray Center (CXC) in the application packages CIAO and ChIPS.

APPENDIX A: *SWIFT* IMAGES

Both the radio hotspot 3C 105 South and 3C 445 South have been detected by *Swift* in the energy range 0.3-10 keV. The reduction procedure for *Swift* data follows that described in Massaro et al. (2008). In the following we report only the basic details.

3C 105 has been observed by *Swift* in four occasions (Obs. ID 00035625001-2-3-4) for a total exposure of ~ 22 ks while 3C 445 only for ~ 12 ks (Obs. ID 00030944001-2). During all these observations, the *Swift* satellite was operated with all the instruments in data taking mode. We consider only XRT (Burrows et al. 2005) data, since our sources were not bright enough to be detected by the BAT high energy experiment. In particular, *Swift*-XRT observations have been performed in photon-counting mode (PC).
The XRT data analysis has been performed with the XRT-DAS software, developed at the ASI Science Data Center (ASDC) and distributed within the HEAsoft pack- age (v. 6.9). Event files were calibrated and cleaned with standard filtering criteria using the xrtpipeline task, combined with the latest calibration files available in the *Swift* CALDB distributed by HEASARC. Events in the energy range 0.3-10 keV with grades 0-12 (PC mode) were used in the analysis (see Hill et al. 2004 for more details). No signatures of pile-up were found in our *Swift* XRT observations. Events are extracted using a 17 arcsec radius circle centered on the radio position of the southern hotspots in both cases of 3C 105 and 3C 445 (see Fig. A1). we measured 15 counts in the southern hotspot of 3C 105 and 12 counts for that of 3C 445, while the background estimated from a nearby source-free circular region of the same radius is 1.8 counts and 0.9 respectively.

Figure A1. The *Swift* images (0.3-10 keV) of 3C 105 and 3C 445 are superimposed to the radio contours at 8.4 GHz, for 3C 105 (*top*), and at 1.4 GHz for 3C 445 (*bottom*). First contour level is 3.7 mJy/beam and 3.2 mJy/beam for 3C 105 and 3C 445 respectively. Contour levels increase by a factor of 3.

REFERENCES

Brunetti, G., Setti, G., Comastri, A. 1997, A&A, 325, 898

Brunetti, G., Bondi, M., Comastri, A., Setti, G., 2002, A&A, 381, 795

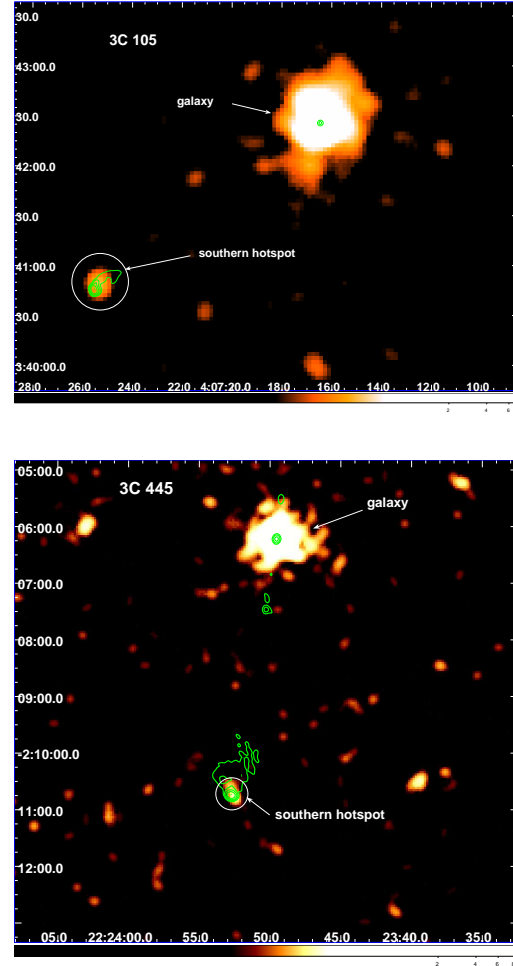Brunetti, G., Mack, K.-H., Prieto, M.A., Varano, S. 2003, MNRAS, 345, 40

Burrows, D., Hill, J.E., Nousek, J.A., et al. 2005, SSRv, 120, 165

Celotti, A., Ghisellini, G., Chiaberge, M. 2001, MNRAS 321, L1

Cox, C.I, Gull, S.F., Scheuer, P.A.G. 1991, MNRAS, 252, 558

Cheung, C.C., Wardle, J.F.C., Chen, T. 2005, ApJ, 628, 104

Eracleous, M., Halpern, J.P. 1994, ApJS, 90, 1

Fanaroff, B.L., Riley, J.M. 1974, MNRAS, 167, 31

Hardcastle, M.J., Harris, D.E., Worrall,D.M., Birkinshaw, M. 2004, ApJ, 612, 729

Hardcastle, M.J., Croston, J.H., Kraft, R.P. 2007, ApJ, 669, 893

Hardcastle, M.J., Cheung, C.C., Feain, I.J., Stawarz, Ł. 2009, MNRAS,393, 1041

Hill, J.E., Burrows, D.N., Nousek, J.A., et al., 2004, SPIE, 5165, 217

Jester, S., Meisenheimer, K., Martel, A.R., Perlman, W., Sparks, W.B., 2007, MNRAS, 380, 828

Kalberla, P.M.W., Burton, W.B., Hartmann, D., Arnal, E.M., Bajaja, E., Morras, R., Pöppel, W.G.L., 2005, A&A, 440, 775

Lähteenmäki, A., Valtaoja, E. 1999, AJ, 117, 1168

Leahy, J.P., Black, A.R.S., Dennett-Thorpe, J., et al. 1997, MNRAS, 291, 20

Mack, K.-H., Prieto, M.A., Brunetti, G., Orienti, M. 2009, MNRAS, 392, 705

Massaro, F., Tramacere, A., Cavaliere, A., Perri, M., Giommi, P., 2008, A&A, 478, 395

Massaro, F., Harris, D.E., Chiaberge, M., Grandi, P., Macchetto, F.D., Baum, S.A., O'Dea, C.P., Capetti, A., 2009, ApJ, 696, 980

Massaro, F., Harris, D.E., Tremblay, G.R., et al., 2010, ApJ, 714, 589

Meisenheimer, K., Röser, H.-J., Hiltner, P.R., Yates, M.G., Longair, M.S., Chini, R., Perley, R.A. 1989, A&A, 219, 63

Meisenheimer, K., Yates, M.G., Röser, H.-J. 1997, A&A, 325, 57

Neff, S.G., Roberts, L., Hutchings, J.B. 1995, ApJS, 99, 349

Perlman, E.S., Georganopoulos, M., May, E.M., Kazanas, D., 2010, ApJ, 708, 1

Prieto, M.A., Kotilainen, J.K. 1997, ApJ, 491, 77

Prieto, M.A., Brunetti, G., Mack, K.-H. 2002, Science, 298, 193

Readhead, A.C.S. 1994, ApJ, 426, 51

Tavecchio, F., Maraschi, L., Sambruna, R.M., Urry, C.M. 2000, ApJ 544, L23

Tadhunter, C.N., Morganti, R., di Serego Alighieri, S., Fosbury, R.A.E., Danziger, I.J. 1993, MNRAS, 263, 999

Thomson, R.C., Crane, P., MacKay, C.D. 1995, ApJ, 446, 93

Tingay, S.J., Lenc, E., Brunetti, G., Bondi, M. 2008, AJ, 136, 2473

Williams, A.G., Gull, S.F. 1985, Nature, 313, 34